The Planetary Science Journal, 3:123 (16pp), 2022 May https://doi.org/10.3847/PSJ/ac66eb

Apophis Planetary Defense Campaign

Vishnu Reddy[1], Michael S. Kelley[2], Jessie Dotson[3], Davide Farnocchia[4], Nicolas Erasmus[5], David Polishook[6], Joseph Masiero[7], Lance A. M. Benner[4], James Bauer[8], Miguel R. Alarcon[9,10], David Balam[11], Daniel Bamberger[12], David Bell[13], Fabrizio Barnardi[14], Terry H. Bressi[1], Marina Brozovic[4], Melissa J. Brucker[1], Luca Buzzi[15], Juan Cano[16], David Cantillo[1], Ramona Cennamo[16], Serge Chastel[17], Omarov Chingis[18], Young-Jun Choi[19,20], Eric Christensen[1], Larry Denneau[17], Marek Dróżdż[21], Leonid Elenin[22], Orhan Erece[23,24], Laura Faggioli[16], Carmelo Falco[25], Dmitry Glamazda[26], Filippo Graziani[27], Aren N. Heinze[17], Matthew J. Holman[13], Alexander Ivanov[28], Cristovao Jacques[29], Petro Janse van Rensburg[5,30], Galina Kaiser[26], Krzysztof Kamiński[31], Monika K. Kamińska[31], Murat Kaplan[23], Dong-Heun Kim[19,36], Myung-Jin Kim[19], Csaba Kiss[32], Tatiana Kokina[33], Eduard Kuznetsov[26], Jeffrey A. Larsen[34], Hee-Jae Lee[19], Robert C. Lees[30], Julia de León[9], Javier Licandro[9,10], Amy Mainzer[1], Anna Marciniak[31], Michael Marsset[35], Ron A. Mastaler[1], Donovan L. Mathias[3], Robert S. McMillan[1], Hissa Medeiros[9,10], Marco Micheli[16], Artem Mokhnatkin[22], Hong-Kyu Moon[19], David Morate[9], Shantanu P. Naidu[4], Alessandro Nastasi[25], Artem Novichonok[37], Waldemar Ogłoza[21], András Pál[32,38,39], Fabricio Pérez-Toledo[9], Alexander Perminov[26], Elisabeta Petrescu[40], Marcel Popescu[41], Mike T. Read[1], Daniel E. Reichart[42], Inna Reva[18], Dong-Goo Roh[19], Clemens Rumpf[3], Akash Satpathy[1], Sergei Schmalz[22], James V. Scotti[1], Aleksander Serebryanskiy[18], Miquel Serra-Ricart[9,10], Eda Sonbas[43], Robert Szakáts[32], Patrick A. Taylor[44], John L. Tonry[17], Andrew F. Tubbiolo[1], Peter Veres[13], Richard Wainscoat[17], Elizabeth Warner[8], Henry J. Weiland[17], Guy Wells[45], Robert Weryk[17], Lorien F. Wheeler[3], Yulia Wiebe[26], Hong-Suh Yim[19], Michał Żejmo[46], Anastasiya Zhornichenko[22], Stanisław Zoła[21,47], and Patrick Michel[48]

[1] Lunar and Planetary Laboratory, University of Arizona, Tucson, AZ 85721, USA; vishnureddy@arizona.edu
[2] Planetary Defense Coordination Office, Planetary Science Division, NASA Headquarters, Washington, DC 20546, USA
[3] NASA Ames Research Center, Moffett Field, CA 94035, USA
[4] Jet Propulsion Laboratory, California Institute of Technology, Pasadena, CA 91109, USA
[5] South African Astronomical Observatory, Cape Town, 7925, South Africa
[6] Faculty of Physics, Weizmann Institute of Science, Rehovot 7610001, Israel
[7] Caltech/IPAC, Pasadena, CA 91125, USA
[8] Department of Astronomy, University of Maryland, College Park, MD 20742, USA
[9] Instituto de Astrofísica de Canarias, C/Vía Láctea s/n, E-38205 La Laguna, Canarias, Spain
[10] Departamento de Astrofísica, Universidad de La Laguna, E-38205 La Laguna, Canarias, Spain
[11] University of Victoria, Victoria, BC, V8W 3P6, Canada
[12] Northolt Branch Observatories, Alfred-Wegener-Straße 34, D-35039 Marburg, Germany
[13] Minor Planet Center, Harvard-Smithsonian Center for Astrophysics, Cambridge, MA 02138, USA
[14] SpaceDyS s.r.l., I-56023 Navacchio di Cascina (PI), Italy
[15] Società Astronomica Schiapparelli, I-21100 Varese, Italy
[16] ESA NEO Coordination Centre, I-00044 Frascati (RM), Italy
[17] Institute for Astronomy, University of Hawaii, Honolulu, HI 96822, USA
[18] Fesenkov Astrophysical Institute, 050020 Almaty, Kazakhstan
[19] Korea Astronomy and Space Science Institute, 776 Daedeok-daero, Yuseong-gu, Daejeon 34055, Republic of Korea
[20] University of Science and Technology, 217, Gajeong-ro, Yuseong-gu, Daejeon 34113, Republic of Korea
[21] Mt. Suhora Observatory, Pedagogical University, Podchorążych 2, 30-084, Cracow, Poland
[22] Keldysh Institute of Applied Mathematics of the Russian Academy of Sciences, Moscow, 125047, Russia
[23] Department of Space Sciences and Technologies, Faculty of Science, Akdeniz University, 07058, Antalya, Turkey
[24] TUBITAK National Observatory, Akdeniz University Campus, 07058 Antalya, Turkey
[25] GAL Hassin, Centro Internazionale per le Scienze Astronomiche, I-90010 Isnello (PA), Italy
[26] Kourovka Astronomical Observatory, Institute of Natural Sciences and Mathematics, Ural Federal University, Ekaterinburg, 620000, Russia
[27] GAUSS Srl, I-00138 Rome, Italy
[28] Kuban State University, Krasnodar, 350040, Russia
[29] Southern Observatory for Near Earth Asteroids Research, Morro do Diamante, Oliveira, Minas Gerais, 35540, Brazil
[30] Department of Astronomy, University of Cape Town, Rondebosch, 7701, South Africa
[31] Astronomical Observatory Institute, Faculty of Physics, A. Mickiewicz University, Słoneczna 36, 60-286 Poznań, Poland
[32] Konkoly Observatory, Research Centre for Astronomy and Earth Sciences, Hungarian Academy of Sciences, Konkoly Thege Miklós út 15-17, H-1121 Budapest, Hungary
[33] Universidad Autónoma de Sinaloa, 80040 Culiacán Rosales, Sin., Mexico
[34] United States Naval Academy, Annapolis, MD 21402, USA
[35] Department of Earth, Atmospheric and Planetary Sciences, MIT, Cambridge, MA 02139, USA
[36] Chungbuk National University, 1 Chungdae-ro, Seowon-gu, Cheongju, Chungbuk 28644, Republic of Korea
[37] Petrozavodsk State University, Petrozavodsk, 185035, Russia
[38] Eötvös Loránd University, H-1117 Pázmány Péter sétány 1/A, Budapest, Hungary
[39] MIT Kavli Institute for Astrophysics and Space Research, 70 Vassar Street, Cambridge, MA 02109, USA
[40] ESA ESOC, Robert-Bosch-Straße 5, D-64293 Darmstadt, Germany
[41] Astronomical Institute of the Romanian Academy, 5, Cutitul de Argint, 040557 Bucharest, Romania
[42] University of North Carolina at Chapel Hill, Chapel Hill, North Carolina NC 27599, USA
[43] University of Adiyaman, Department of Physics, 02040 Adiyaman, Turkey
[44] Lunar and Planetary Institute, Universities Space Research Association, Houston, TX 77058 USA
[45] Northolt Branch Observatories, Northolt, Middlesex, UB5 4AG, UK
[46] Kepler Institute of Astronomy, University of Zielona Góra, Lubuska 2, 65-265 Zielona Góra, Poland
[47] Astronomical Observatory, Jagiellonian University, ul. Orla 171, 30-244 Cracow, Poland

[48] Observatoire de la Côte d'Azur, BP 4229, F-06304 Nice Cedex 4 France
Received 2021 December 22; revised 2022 April 3; accepted 2022 April 5; published 2022 May 31

Abstract

We describe results of a planetary defense exercise conducted during the close approach to Earth by the near-Earth asteroid (99942) Apophis during 2020 December–2021 March. The planetary defense community has been conducting observational campaigns since 2017 to test the operational readiness of the global planetary defense capabilities. These community-led global exercises were carried out with the support of NASA's Planetary Defense Coordination Office and the International Asteroid Warning Network. The Apophis campaign is the third in our series of planetary defense exercises. The goal of this campaign was to recover, track, and characterize Apophis as a potential impactor to exercise the planetary defense system including observations, hypothetical risk assessment and risk prediction, and hazard communication. Based on the campaign results, we present lessons learned about our ability to observe and model a potential impactor. Data products derived from astrometric observations were available for inclusion in our risk assessment model almost immediately, allowing real-time updates to the impact probability calculation and possible impact locations. An early NEOWISE diameter measurement provided a significant improvement in the uncertainty on the range of hypothetical impact outcomes. The availability of different characterization methods such as photometry, spectroscopy, and radar provided robustness to our ability to assess the potential impact risk.

Unified Astronomy Thesaurus concepts: Near-Earth objects (1092); Asteroids (72); Small Solar System bodies (1469); Close encounters (255)

1. Introduction

Impacts due to Near-Earth Objects (NEOs) are the only natural hazard that can be prevented if the threat is detected with sufficient lead time. NASA's Planetary Defense Coordination office (PDCO) was established in part with the goal of coordinating global planetary defense assets in the event such a threat is identified. Planetary defense campaigns test the operational readiness of the global coalition of observers, modelers, and decision-makers to tackle a potential NEO impact hazard. Since 2017, we have conducted three such campaigns, each with a specific set of objectives. These campaigns were carried out under the auspices of the International Asteroid Warning Network (IAWN), which was established by the United Nations in 2013 to coordinate organizations involved in detecting, tracking, and characterizing NEOs. IAWN is tasked with developing well-defined communication plans and protocols to assist governments in the analysis of asteroid impact consequences and in the planning of mitigation responses.

As a first exercise in 2017, we observed Near-Earth asteroid (NEA) 2012 TC4 with the primary goal of recovering and characterizing the ~20 m object (Chelyabinsk impactor size) using an array of ground- and space-based optical, infrared, and radar assets (Reddy et al. 2019). A key finding of the TC4 campaign was that NEA characterization was not at the same operational readiness level as astrometry and hazard modeling. As a proposed follow-up to the TC4 campaign, our second campaign focused on NEA characterization in order to improve the operational readiness of characterization efforts. The target of this second campaign was the binary NEA (66391) Moshup, originally designated as 1999 KW4, which passed close to Earth in 2019 May. A key finding was that the binary nature of the target had very little effect on the impact risk on the ground (Reddy et al. 2022). This was due to the large size of Moshup (the primary) relative to Squannit (the secondary), which is typical for binary systems formed by the YORP effect (see Pravec et al. 2006). Hence, the effective diameter (and impact energy) of the system is dominated by the primary with little contribution from the secondary.

Apophis was chosen as a target for the third exercise because the 2020–2021 apparition was the last opportunity to observe this target before the exceptionally close encounter in 2029 (Brozović et al. 2018). The goal of this campaign was to recover, track, and characterize Apophis as a potential impactor in order to exercise the planetary defense system from observations to hypothetical risk assessment and prediction, and communication. This campaign included participation by amateur and professional astronomers from around the world and was conducted from 2020 October through 2021 April. As with the previous campaigns, we treated Apophis as an unknown object, thus any previously published information about the target was not included in this exercise. By treating Apophis as a new object, we were able to quantify the operational efficiency of each working group in delivering the observational input to the hypothetical risk assessment working group. It should be noted that, as participation in this campaign was on a voluntary basis, there were other observers taking data of Apophis at the time of the campaign, which is not included here. In a real impactor situation, these data would also be available for hazard analysis.

Here, we present an overview of the campaign and summarize the operational results. Our goal is to share information about our efforts to derive operationally relevant data products in a timely manner. The Apophis campaign followed protocols that were refined based on experience from the two previous exercises. Campaign participation was voluntary, with nearly 100 participants from 18 nations. The team was divided into working groups depending on the observational technique (astrometry, photometry, visible and thermal infrared spacecraft observations, visible/near-infrared spectroscopy, and radar) or task at hand (hypothetical risk assessment). The observation working groups provided derived target parameters (e.g., orbit, size, albedo, and composition), which were used as input parameters to the hypothetical risk assessment model. Impact hazard models were run at four different epochs as new inputs were received from the

working groups. Each assessment epoch reflects significant advancement in the state of knowledge about the impact probability, possible locations of the impacting clone, and the physical properties of Apophis.

2. Astrometry and Orbit Determination

2.1. Discovery of Apophis

We treated Apophis as an unknown object and waited for it to be detected in serendipitous observations from the ongoing asteroid surveys. The surveys reported Apophis observations as unidentified objects and the Minor Planet Center (MPC) intentionally did not attempt to link them to the known orbit of Apophis. On 2020 December 4, the Catalina Sky Survey (Christensen et al. 2018) first detected Apophis and reported the corresponding astrometry to the MPC. To classify newly discovered objects, the MPC uses the digest2 score, which assesses the likelihood that an object is an NEO based on the observed plane-of-sky motion from a short arc of observations and a solar system population model (Keys et al. 2019). Because the plane-of-sky motion from the initial Catalina detections resembled that of more distant main-belt asteroids, the digest2 score used to classify newly discovered objects was lower than 65, which is the threshold for posting a candidate near-Earth object on the NEO Confirmation Page (NEOCP, Marsden & Williams 1998). As a result, the astrometry was added to the MPC's isolated tracklet file (ITF). In the following two weeks, Apophis was observed by Catalina again, as well as by the ATLAS (Tonry et al. 2018) and Pan-STARRS (Wainscoat et al. 2020) surveys, maintaining a low digest2 score due to its main-belt-like motion.

On 2020 December 18 and 19, the NEOWISE survey (observatory code C51; Mainzer et al. 2014) obtained 10 thermal infrared observations of Apophis. Because of the longer time interval covered by NEOWISE tracklet submissions compared to ground-based surveys ($\sim$1 day versus $\sim$1 hr) and to encourage additional observations to obtain visible-light magnitudes, the MPC's standard procedure for unidentified NEOWISE data is different than for other observers. This procedure resulted in Apophis being posted to the NEOCP because of a possible NEO orbit fit to the data, regardless of the digest2 score. Therefore, on 2020 December 22, the 10 NEOWISE astrometric positions were posted on the NEOCP as N00hp15. Within one day, all other previous serendipitous survey observations were linked to the NEOWISE tracklet, and follow-up data were collected by the NEO community at large, for a total of 74 astrometric observations. On 2020 December 23 the MPC announced the pseudo-discovery of Apophis (MPEC 2020-Y98, https://minorplanetcenter.net/mpec/K20/K20Y98.html). Without the MPC special handling of the NEOWISE submission, the periodic analysis of the MPC ITF catalog as described in Weryk et al. (2018) would have identified Apophis on 2020 December 28.

2.2. Tracking Apophis

After the pseudo-discovery, the following surveys regularly observed Apophis over 314 observations. These included:

1. the Catalina Sky Survey (Christensen et al. 2018), observatory codes 703 and G96;
2. ATLAS (Tonry et al. 2018), observatory codes T05 and T08;
3. Pan-STARRS (Wainscoat et al. 2020), observatory codes F51 and F52;
4. the Zwicky Transient Facility (Graham et al. 2019), observatory code I41.
5. the Southern Observatory for Near Earth Asteroids Research (SONEAR), observatory code Y00 (only on 2021 January 21, February 24, and March 2).

In addition to survey observations, the astrometry segment of the Apophis campaign included follow-up observers that contributed observations from the following stations: 094, 168, 186, 204, 291, 691, C40, C53, C73, H06, H78, I52, J04, K91, L28, L34, N42, N82, Q62, V26, Y00 (only on 2021 April 11), Z80, and Z84. There were a total of 1183 follow-up observations from 23 observatories, with 7 in Europe, 5 in Asia, 4 in North America, 2 in South America, and 1 each in Australia and Africa. The observatory names and coordinates are available at https://minorplanetcenter.net/iau/lists/ObsCodesF.html.

The collected optical observations are available in the Daily Orbit Update Minor Planet Electronic Circulars (MPECs) from MPEC 2020-Y109 (https://minorplanetcenter.net/mpec/K20/K20YA9.html) to MPEC 2021-J210 (https://minorplanetcenter.net/mpec/K21/K21JL0.html). Figure 1 shows the daily number of survey and follow-up observations obtained during the observation campaign. Although follow-up observations represent the vast majority of the data set, survey observations alone provide extensive coverage due to the favorable observing circumstances (the V magnitude peaked at $V = 16$ and the maximum solar elongation was 156°).

Radar astrometry is a powerful means of constraining asteroid orbits when obtainable (Ostro et al. 2002). The 0.1 au close approach distance to Earth enabled radar observations of Apophis, which are discussed in more detail in Section 7. Goldstone obtained one Doppler measurement on 2021 March 3 and three delay measurements on 2021 March 5, 8, and 11 (https://ssd.jpl.nasa.gov/?radar).

2.3. Orbit Determination and Impact Hazard Assessment

Starting from the pseudo-discovery, we computed orbit estimates at a weekly cadence using standard least-squares orbit determination techniques (Farnocchia et al. 2015). In particular, we applied the Eggl et al. (2020) star catalog debiasing scheme and data weights from Vereš et al. (2017) to optical astrometry. The optical observation times were assumed to have uncertainties of 1 s. For radar data, we set the data weights based on the reported uncertainties. For the final orbit estimate, optical ground-based and space-based astrometry, radar delay, and Doppler residuals have an rms of 0.″26, 0.″47, 0.23 μs (which corresponds to about 35 m, one way), and 0.07 Hz, respectively.

Even though an Earth impact by Apophis in 2029 had already been ruled out (Chesley 2006), the close approach distance of 38,000 km in 2029 (Giorgini et al. 2008) and the larger uncertainties obtained by assuming that Apophis was a new discovery made an impact trajectory theoretically possible for the campaign. As a proxy for the expected evolution, the blue curve in Figure 2 shows the campaign impact probability for the known 2029 close approach at 38,000 km from the geocenter as a function of the uncertainty in the ζ (zeta) coordinate on the 2029 B-plane. The B-plane is the plane with the geocenter at the origin, orthogonal to the inbound velocity of Apophis relative to Earth, and the $-\zeta$ direction is aligned

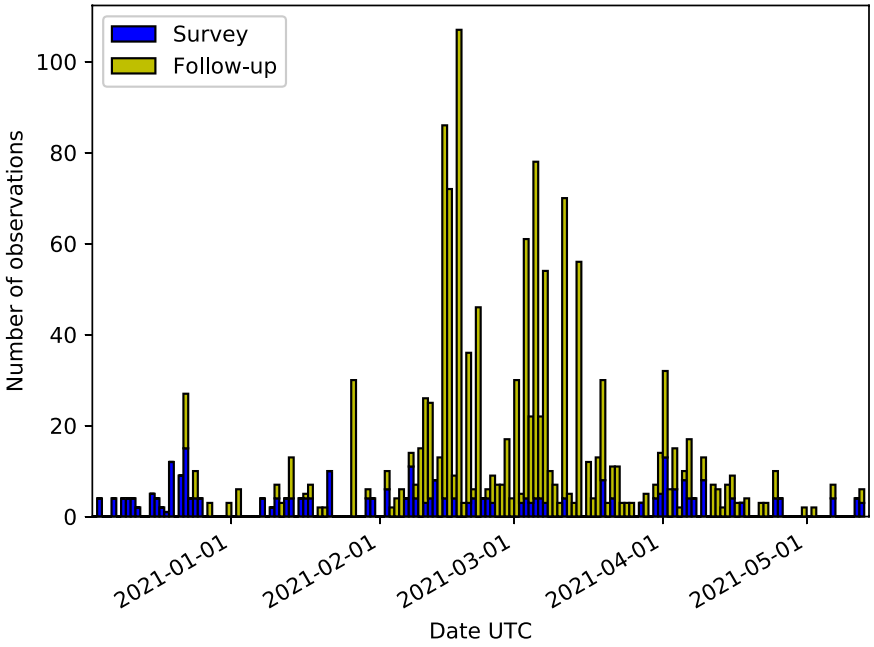

Figure 1. Daily number of observations from surveys and follow-up observers. The follow-up data on 2020 December 22 were collected by the NEO community at large when Apophis was on the NEOCP as N00hp15. For later dates, the count of follow-up data only refers to observations collected as part of the campaign.

with the inertial heliocentric velocity of Earth, thus reflecting the time of arrival at the encounter (Valsecchi et al. 2003). The campaign impact probability initially increased as the uncertainty region shrank and shifted toward Earth. This continued to a peak of 16%, after which Earth started moving toward the tail of the uncertainty distribution, and the impact probability decreased. As Earth fell outside the uncertainty region, the impact was ruled out. If Apophis had been on an impact trajectory, the impact probability would have continued increasing until it reached 100%, as described by the red curve in Figure 2.

For every orbit update, we assessed the probability of an Earth impact in 2029 using both a Monte Carlo approach (Farnocchia et al. 2015) and the Line of Variations method (Milani et al. 2005). The crosses in Figure 2 correspond to the computed impact probabilities over time, which track the theoretical blue curve. The peak (16%) was reached on 2021 February 16, when the ζ uncertainty was 27,000 km. The corresponding values of the Torino scale (Binzel 2000) and Palermo scale (Chesley et al. 2002) were 4 and 2.1, respectively. As the observed arc over the campaign extended further in time, the impact probability dropped and became zero once radar astrometry was collected and lowered the ζ uncertainty to 2000 km.

To support the risk assessment exercise described in Section 8, we considered a hypothetical impacting trajectory close to that of Apophis using the orbital elements in Table 1. This trajectory is compatible with the data acquired from the pseudo-discovery date through 2021 February 2, when we switched to this trajectory in terms of impact analysis. Instead of correcting the orbit solution based on new observational data, we froze the nominal solution and only updated the covariance based on the new observational data to reflect the improved accuracy in our orbital knowledge. The corresponding impact probability evolution is represented by triangles in Figure 2 and reaches 100% once radar astrometry is included. The final Torino scale and Palermo scale of the hypothetical impacting trajectory were 9 and 2.9, respectively.

3. Spacecraft Observations

Two spacecraft missions contributed astrometric and characterization information to the campaign: NASA's Near-Earth Object Wide-field Infrared Survey Explorer (NEOWISE) and the Canadian NEOSSat. Data from these spacecraft were reduced by their respective teams and delivered to the campaign at three epochs.

3.1. NEOWISE

The NEOWISE spacecraft (Mainzer et al. 2014) has been conducting an all-sky thermal infrared survey for asteroids and comets since 2013 December. NEOWISE makes use of the WISE spacecraft (Wright et al. 2010), which is in a low-Earth Sun-synchronous polar orbit and surveys at solar elongations near 90°. Using a beamsplitter, NEOWISE obtains simultaneous images at 3.4 μm and 4.6 μm of a $47' \times 47'$ field of view. NEOWISE observed Apophis at two epochs as it passed through the survey's field of regard, on 2020 December 18–19 and again on 2021 March 31–April 01.

In the first NEOWISE epoch (2020 December), Apophis was detected at 4.6 μm in 10 exposures with a signal-to-noise ratio (S/N) between 5 and 8. These thermal infrared data, in combination with the near-simultaneous visible-light photometry (see Section 5) and the orbit obtained from the discovery and follow-up observations as part of this exercise (see Section 3), were sufficient to perform thermal modeling of Apophis and derive a size and albedo. Based on these measurements, a NEATM thermal model (Harris 1998) was fit to the data following the standard NEOWISE procedure (for details, see Masiero et al. 2020). The preliminary best-fit NEATM model had a spherical-equivalent diameter of 300 ± 75 m and a geometric V-band albedo of 0.44 ± 0.19. This NEOWISE diameter fit was provided to the risk

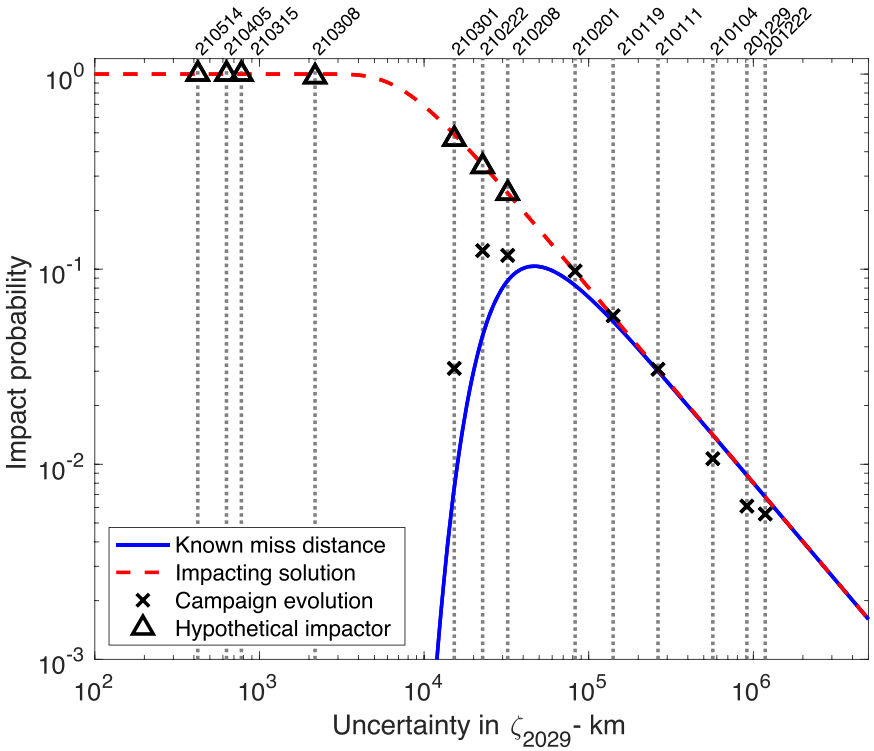

Figure 2. Impact probability evolution as a function of the uncertainty in the ζ coordinate on the 2029 B-plane. The solid curve represents the theoretical evolution with the nominal set of observations to the known 38,000 km miss distance. The dashed curve is the theoretical evolution of an impacting trajectory. The dotted vertical lines mark the orbit updates during the campaign. The crosses represent the corresponding impact probabilities. The triangles correspond to the impacting clone, introduced as the impact probability that departed from the dashed curve. Dates are in the YYMMDD compressed format.

Table 1
Osculating Heliocentric Orbital Elements of the Hypothetical Impacting Clone at Epoch 2020 December 19.0 TDB in the IAU76 Ecliptic frame (Seidelmann 1977)

Eccentricity	0.191 517 960 909 729 1
Perihelion distance	0.745 839 747 905 277 1 au
Time of perihelion	2020-09-08.540620230138 TDB
Longitude of node	204.041 463 298 085 1 deg
Argument of perihelion	126.653 025 089 043 1 deg
Inclination	3.336 865 537 761 929 deg

assessment group approximately 2 hr after the pseudo-discovery was announced.

3.2. NEOSSat

Canada's Near-Earth Object Surveillance Satellite (NEOSSat), jointly operated by the Canadian Space Agency (CSA) and Defence Research & Development Canada (DRDC), is a 75 kg microsatellite launched to Sun-synchronous low-Earth orbit (LEO) in 2013, featuring a 15 cm Maksutov telescope with a 0.85 degree field of view and a plate scale of 3 arcsec/pixel on its 1024×1024 CCD. The close encounter circumstances for Apophis provided a test of the motion compensation routine. Such close encounters are ideal for the NEOSSat platform, as the direct measurement of the parallax is significantly larger than the astrometric noise resulting from the large image scale (3″/pixel). For Apophis, the measured FWHM of the target profile did not deviate, within measurement error, from the FWHM of nearby stars in the field. We were also able to detect the extreme effect of the parallax for an object at a distance of 0.114 au from the spacecraft. Due to the large image scale, the astrometry that was derived from the NEOSSat spacecraft was not used to update Apophis' orbit but did demonstrate a capability to collect space-based astrometric observations of small bodies as part of a planetary defense exercise.

4. Photometry

Campaign photometric observations followed the announcement of the pseudo-discovery of Apophis by asteroid surveys on 2021 December 23. Over the course of the ∼120 days that followed, observations were acquired by the community from sites on six continents spanning a wide range in both latitude and longitude. The observations (36 sources and >19,000 data points) that comprise the photometric campaign are summarized in Table 2. The data were reduced in a standard manner and provided by each contributor as calibrated apparent magnitudes.

Because the campaign spanned several months of observations, with varying observing geometries and Earth–asteroid distances, δ, all observing times were corrected for light-travel time, and the apparent magnitudes were converted to absolute magnitudes before any analysis of the photometric data was performed. Figure 3(A) shows all data in reduced magnitude where the magnitude's dependence on δ has been removed and the reduced magnitudes are plotted as a function of the Earth–Asteroid–Sun observing angle (or phase angle, α). At the start of the campaign, the phase angle was about 70°, and it reached a minimum of ∼20° a few days before the closest approach. After the close approach, the phase angle increased to ∼100° toward the end of the campaign.

Figure 3(A) also shows the H-G model fit in the convention formulated by Bowell et al. (1989) and summarized in Dymock (2007). The value of the slope parameter, G, and absolute

Table 2
Summary of Optical Photometric Observations

Observatory and Telescope	Aper. Size (m)	Location	Filters	Number of Data Points	Observation Window
Meckering Observatory (PROMPT-MO-1)	0.4	Australia	*R*	21	2021-02-12–2021-02-22
Siding Spring Observatory (KMTNet-SSO)	1.6	Australia	*B*, *V*, *R*, and *I*	41	2021-03-03–2021-04-20
Cerro Tololo Inter-American Observatory (PROMPT 5 & 6)	0.4	Chile	*R*	18	2021-02-08–2021-03-17
Cerro Tololo Inter-American Observatory (KMTNet-CTIO)	1.6	Chile	*B*, *V*, *R*, and *I*	15	2021-03-03–2021-04-03
Northolt Branch Observatories (0.25 m)	0.25	England	clear	365	2021-02-28–2021-03-17
Space Observatory (TESS)	0.1	High Earth Orbit	TESS	1248	2021-02-19–2021-03-06
Wise Observatory (28 inch)	0.7	Israel	clear	710	2020-12-24–2021-04-04
Wise Observatory (OWL-Net3)	0.5	Israel	*R*	29	2021-02-10–2021-03-19
GAL Hassin Astronomical Center (GRT1)	0.4	Italy	clear	55	2021-03-30–2021-03-30
Tien-Shan Astronomical Observatory (1 m)	1.0	Kazakhstan	*R*	363	2021-01-26–2021-03-19
Mount Suhora Observatory (0.6 m)	0.6	Poland	*R*	194	2021-02-20–2021-03-13
Jagiellonian University Astronomical Observatory (0.5 m)	0.5	Poland	*R*	122	2021-03-06–2021-03-15
Kourovka Astronomical Observatory (0.4 m)	0.4	Russia	*R* and *V*	346	2021-02-10–2021-03-22
Simeiz Observatory (Zeiss-1000)	1.0	Russia/Ukraine	clear, *R*, and *V*	187	2021-03-07–2021-03-07
Calar Alto Observatory (Schmidt)	0.8	Spain	*V* and *g*	8475	2021-01-13–2021-04-05
Teide Observatory (TAR4)	0.4	Spain	clear	327	2021-03-16–2021-03-23
Teide Observatory (TAR2)	0.5	Spain	clear	507	2021-01-21–2021-03-21
Teide Observatory (IAC80)	0.8	Spain	*R*	328	2021-01-19–2021-02-25
South African Astronomical Observatory (Lesedi)	1.0	South Africa	*V*	651	2021-01-29–2021-02-10
South African Astronomical Observatory (40-inch)	1.0	South Africa	*R*	7	2021-02-24–2021-02-25
South African Astronomical Observatory (KMTNet-SAAO)	1.6	South Africa	*B*, *V*, *R*, and *I*	59	2021-03-03–2021-04-18
Sobaeksan Optical Astronomy Observatory (0.6 m)	0.6	South Korea	*R*	182	2021-02-18–2021-03-10
Bohyunsan Optical Astronomy Observatory (1.8 m)	1.8	South Korea	*R*	123	2021-02-19–2021-03-16
Daedeok Observatory (OWL-Net0)	0.5	South Korea	*R*	57	2021-02-22–2021-02-22
Bohyunsan Optical Astronomy Observatory (OWL-Net5)	0.5	South Korea	*R*	8	2021-02-19–2021-02-22
Adiyaman University Observatory (T60)	0.6	Turkey	*R*	23	2021-03-16–2021-03-16
TÜBİTAK National Observatory (T100)	1.0	Turkey	clear, *B*, *V*, *R*, and *I*	511	2021-03-01–2021-03-13
Haleakala Observatory (ATLAS-HKO)	0.5	USA	*c* and *o*	56	2020-12-24–2021-05-01
Mauna Loa Observatory (ATLAS-MLO)	0.5	USA	*c* and *o*	117	2020-12-24–2021-05-03
Winer Observatory (RBT)	0.7	USA	*R*	271	2021-02-11–2021-03-12
Steward Observatory (Spacewatch 1.8 m)	1.8	USA	OG-515	477	2021-01-08–2021-01-18
Steward Observatory (Spacewatch 0.9 m)	0.9	USA	OG-515	2116	2021-02-05–2021-04-13
UMD Astronomy Observatory (7-inch)	0.18	USA	*R*	404	2021-03-06–2021-03-07
Mt. Lemmon Optical Astronomy Observatory (1.0 m)	1.0	USA	*R*	511	021-01-16–2021-03-16
Mt. Lemmon Optical Astronomy Observatory (OWL-Net4)	0.5	USA	*R*	734	2021-02-06–2021-03-22
Kitab Observatory (0.36 m)	0.36	Uzbekistan	clear	275	2021-02-14–2021-02-17

magnitude, $H_V(\alpha = 0)$, from the model fit on the campaign data, 0.24 ± 0.12 and 19.20 ± 0.28, respectively, are shown in the top-right corner of Figure 3(A). The *V*-filter data together with the custom ATLAS *c*-filter and Sloan *g*-filter data from the campaign were used for the H-G model fit because the $V - c$ and $V - g$ colors for the campaign data were only 0.03 and −0.10 mag, respectively (i.e., $c \approx g \approx V$). During the campaign, no data were collected at phase angles below 20°, which is essential for reliable phase-curve fitting, and therefore, the *G* value for the fit shown in Figure 3(A) was restricted to a typical S-type asteroid's expected value of $G = 0.24$ (Vereš et al. 2015). The campaign-derived absolute magnitude value was $H_V = 19.20 \pm 0.28$, which was used to constrain the visible-light geometric albedo during the NEOWISE thermal infrared diameter determination (Section 3.1).

Before performing any rotation period analysis, all filter data were offset to match the *V*-filter magnitudes by subtracting/adding the relevant campaign-derived colors (see text in the paragraph that follows). A rotation period search was performed on the entire photometry data set with the SciPy (Virtanen et al. 2020) implementation of the Lomb–Scargle method (LS; Lomb 1976; Scargle 1982), searching for periods between 1 and 2000 hr. The resulting LS periodogram (Figure 3(B)) shows the strongest peak at a rotation period of $P = 30.55 \pm 0.12$ hr (an asteroid's rotation period is double that of the single-sinusoid lightcurve period). This period is

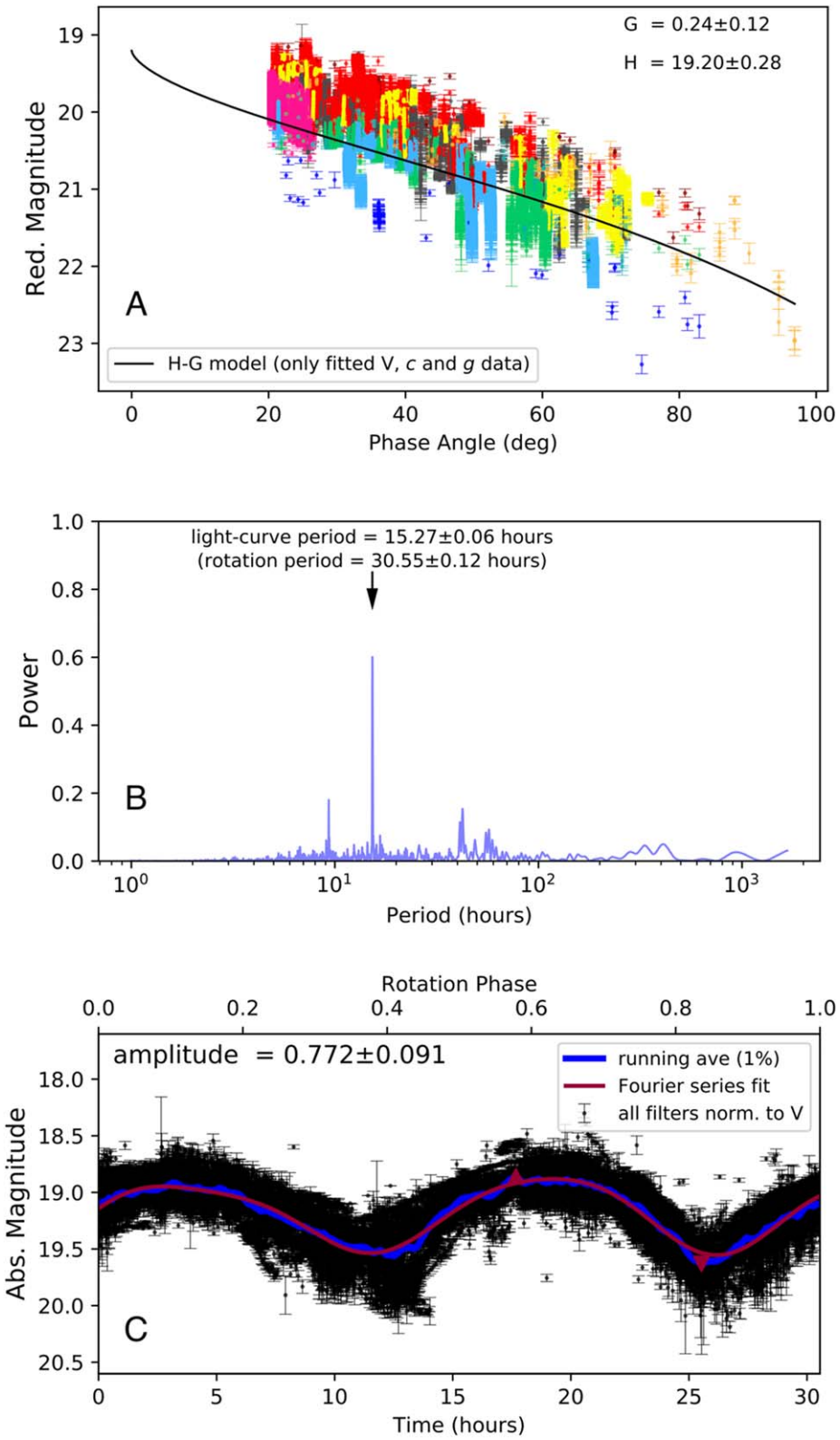

Figure 3. (A) Photometric reduced magnitude with the observer-to-object distance dependence on the brightness removed. The H-G model fit is shown, with the derived G and H_V values shown in the top-right corner. (B) The Lomb–Scargle periodogram of the combined filter data. The arrow shows the strongest periodogram peak with the lightcurve period (i.e., half the rotation period) and the rotation period labeled. The rotation period of $P = 30.55 \pm 0.12$ hr matches the strongest lightcurve amplitude for the second harmonic of the period. (C) The combined photometric data folded with the best period solution and with a Fourier series fit shown as a solid burgundy line. The burgundy triangles show the minimum and maximum values of the fit and are used to determine the lightcurve amplitude displayed in the top-left corner of the panel.

Table 3
Observation Circumstances for Visible and Near-IR Spectral Observations

Date [UT]	Midtime UT	Telescope	Exp. Time [min]	Air Mass	Phase Angle [deg]	V_{mag}	Solar Analog
2021-01-26	04:25	GTC	15	1.49	50.7	17.3	SA102-1081
2021-01-14	14:25	IRTF	36	1.28	59.9	17.8	SA98-978SA102-1081

reasonably close to the strongest literature lightcurve amplitude for the second harmonic of the period, $P = (P_{\varphi}{}^{-1} - P_{\psi}{}^{-1})^{-1}$ where $P_{\varphi} = 27.38 \pm 0.07$ hr and $P_{\psi} = 263 \pm 6$ hr are the precession and rotation periods of a moderately excited Short Axis Mode tumbling asteroid (Pravec et al. 2014). The entire campaign's photometry data (~19,000 data points), folded at that best-fit period of $P = 30.55$ hr, are shown in Figure 3(C). The periodogram displays two other minor but distinct peaks at 18.7 and 84.0 hr that are both at N-day alias periods, where $P_{\rm alias} = {\rm abs}(24/(((24)/30.55)+N))$ and $N = -0.5$ and $+0.5$ for these two specific peaks. The relatively large scatter visible in the folded data is due to the lightcurve amplitude variability as a function of observing geometry across the campaign (there is a $>100^{\circ}$ phase-angle spread in the campaign data set). The average lightcurve amplitude is 0.77 ± 0.09 magnitude, indicating that Apophis is likely elongated.

Apophis colors from the campaign data were calculated by using the median magnitude of the combined data in a specific filter relative to the median magnitude value for all the V-filter data. The sparse ATLAS observations with the custom c- and o-filter data provided a campaign-derived $c - o$ color within the first 10 days of the campaign. The initial $c - o$ color already showed a relatively "red" object hinting at an S-type taxonomy. The values calculated were $B - V = 0.818 \pm 0.015$, $V - R = 0.521 \pm 0.003$, $V - I = 0.693 \pm 0.013$, and $c - o = 0.39 \pm 0.03$. The $c - o$ color agrees with a typical S-like $c - o$ color of 0.39 ± 0.01 (versus 0.25 ± 0.01 for a C-like asteroid) reported by Erasmus et al. (2020). The $B - V$, $V - R$, and $V - I$ colors closely resemble those of a typical S-type asteroid with $B - V$, $V - R$, and $V - I$ colors reported in the literature of ~0.85, ~0.48, and ~0.89, respectively (Shevchenko & Lupishko 1998; Dandy et al. 2003; Erasmus et al. 2018). However, the campaign colors better match the colors of a typical Q-type asteroid reported by Dandy et al. (2003) of 0.82, 0.42, and 0.73 for $B - V$, $V - R$, and $V - I$, respectively. The colors derived from the campaign data are in good agreement with the Sq-type spectra also obtained during the campaign.

5. Spectral Observations

Apophis' reflectance spectrum in visible and near-IR wavelengths was measured for the campaign in order to exercise the ability to collect the data, reduce, and analyze it rapidly. The reflectance spectrum helps constrain the asteroid's spectral type, composition, and (indirectly) density, which are crucial parameters for calculating possible damage upon impact or designing a mitigation plan. Visible-wavelength spectra were obtained using the OSIRIS camera spectrograph on the 10.4 m Gran Telescopio Canarias (GTC), located at the El Roque de Los Muchachos Observatory in La Palma, Spain. Observations were obtained using a long slit with 1.″2 width and the R300R grism that provided a wavelength coverage from 0.48 to 0.92 μm. The slit was aligned with the parallactic angle in order to minimize the losses due to atmospheric dispersion. A total of three individual spectra were obtained, applying consecutive offsets of 10″ in the slit direction between each of the 5 minute exposures. Observational details are shown in Table 3. Data reduction was done using standard procedures (see de León et al. 2016).

The campaign also obtained near-infrared (0.8–2.5 μm) spectral observations using SpeX, an imager and spectrograph mounted on the 3.2 m NASA Infrared Telescope Facility (IRTF). We used a long slit with a 0.″8 width and shifted the object along it between two positions (following an A–B–B–A sequence) to allow the subtraction of the background noise. The observations were limited to low air mass values between 1 to 1.6 to reduce chromatic refraction, which can change the spectral slope. The exposure time was 2 minutes per image, and the entire nightly sequence lasted 36 minutes. The MIT Optical Rapid Imaging System (MORIS) camera, which collects visible light after it passes through a dichroic, was used simultaneously to improve the guiding. The observational details are listed in Table 3. The reduction of the raw SpeX images follows standard procedures (e.g., Polishook et al. 2014; Binzel et al. 2019).

The near-IR reflectance spectrum was normalized relative to the visible reflectance spectrum using the data at the wavelength range shared by both measurements (0.8 to 0.9 μm). Figure 4(A) shows the combined visible and near-IR reflectance spectrum of Apophis. We first compared the spectrum to common taxonomic types such as C, S, and X types. As demonstrated in Figure 4(A), the spectrum is closest to an S-type taxonomy. To further refine the taxonomic classification, we compare the Apophis spectrum with subclasses of the S-complex taxonomies including S, Sq, and Q types. Figure 4(B) shows that the reflectance spectrum most closely matches the Sq-type classification of the Bus-DeMeo taxonomy, a common classification (~20% of NEOs; Binzel et al. 2019). Particles sampled by the Hayabusa spacecraft from NEA (25143) Itokawa, which was classified from Earth as an Sq-type body (Binzel et al. 2001), were identified as compositionally similar to the ordinary chondrites (Nakamura et al. 2011). The Sq-type taxonomic classification of Apophis would imply an albedo value of ~0.2 based on previously measured relationships between taxonomic class and albedo (Pravec et al. 2012; Mainzer et al. 2011), which is somewhat lower than the thermal IR measurement by NEOWISE (Section 3.1). This is not unexpected, as the relationship between taxonomic type and albedo can have a large scatter. The Sq-type classification matches the results of previously published spectral measurements of Apophis taken at past apparitions (Binzel et al. 2009; Reddy et al. 2018).

6. Radar Observations

Radar observations of Apophis in 2021 occurred daily between March 3 and 11 and were conducted with the primary goals of obtaining range measurements to reduce uncertainties in the orbit, obtaining echo power spectra and delay-Doppler images to improve constraints on the dimensions of the asteroid and estimating its spin state. We conducted monostatic observations that used the 70 m Goldstone antenna to both transmit (8560 MHz, 3.5 cm) and receive and bistatic

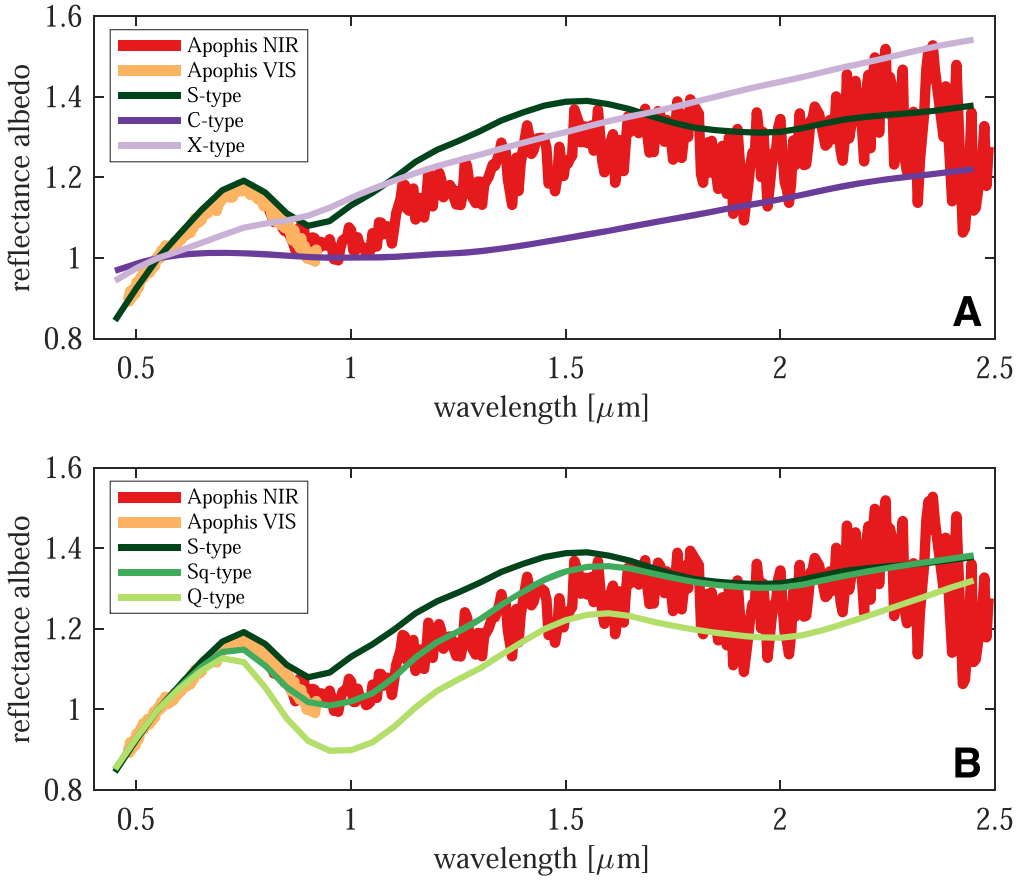

Figure 4. (A) The visible and near-IR reflectance spectrum of Apophis compared to spectra of average S-, C-, X-complex asteroids. Apophis' spectrum resembles S types rather than C or X types. (B) Comparison of Apophis' spectrum to S-complex taxonomic classes. The Apophis spectrum is similar to Sq types, indicating an affinity to LL-chondrite meteorites.

observations in which Goldstone transmitted and the 100 m Green Bank Telescope received. The bistatic configuration doubles the integration time relative to monostatic observations and, combined with the larger aperture of Green Bank, increases the S/N by a factor of about 2. Due to the asteroid's distance of ∼0.11 au and its small diameter of ∼0.34 km, Apophis was a weak radar target at Goldstone in 2021, and the S/N increase provided by a reception at Green Bank was crucial to obtain delay-Doppler images.

Observations had also been planned at Arecibo starting in mid-March when Apophis moved north into Arecibo's decl. window but were not possible following the collapse of the telescope in 2020 December. The radar observations discussed here emphasize the large-scale properties of Apophis and are tailored for the 2021 Apophis planetary defense exercise. Considerably more detailed analysis, 3D shape modeling, and spin-state estimation will appear in a future paper.

The first goal of the observations was to detect echoes and to estimate radar astrometry. We began with monostatic continuous-wave (CW) observations on March 3, which provided a detection with a Doppler correction of 0 Hz that was provided to the Astrometry Working Group (see Section 1) to include in the orbital solution. This Doppler measurement did not change JPL/Horizons orbital solution 202, which we used during the observations and which incorporated astrometry dating back to 2004. However, for the purposes of the Apophis exercise, which used astrometry obtained only since late 2020, the measurement was useful in constraining the orbit. On March 5, we obtained a time delay (range) correction of $+3.5 \pm 1.0$ μs (525 ± 150 m) to JPL/Horizons solution 202; this correction is only slightly larger than the asteroid and significantly less than the 1σ time delay uncertainty of 17 μs (2.55 km). Although a small correction to the ephemeris, this measurement (combined with the full astrometric data set dating back to 2004) improved the orbit sufficiently to rule out any remaining chance of an Earth impact in 2068.

The Doppler broadening or bandwidth of an echo is given by

$$B = 4\pi D \cos(\delta)/(\lambda P),$$

where δ is the subradar latitude, λ is the wavelength of the observations, and P is the rotation period. For a sphere, D is the diameter, but for an irregularly shaped asteroid, D is the pole-on breadth on the plane of the sky at the time of the observations. For an elongated asteroid, the bandwidth can vary considerably as the asteroid rotates. If an estimate of the rotation period is available, then measurements of the bandwidth place lower bounds on the pole-on breadth if the pole direction is unknown and direct estimates on the dimensions if the pole is available.

The initial bandwidth of ∼1 Hz on March 3 (Figure 5) was broadly consistent with expectations given the 30.55 hr period estimated from the photometry during the 2020–2021 campaign (see Section 5) and with the preliminary diameter of 300 ± 75 m (See Section 3.1) estimated from thermal infrared

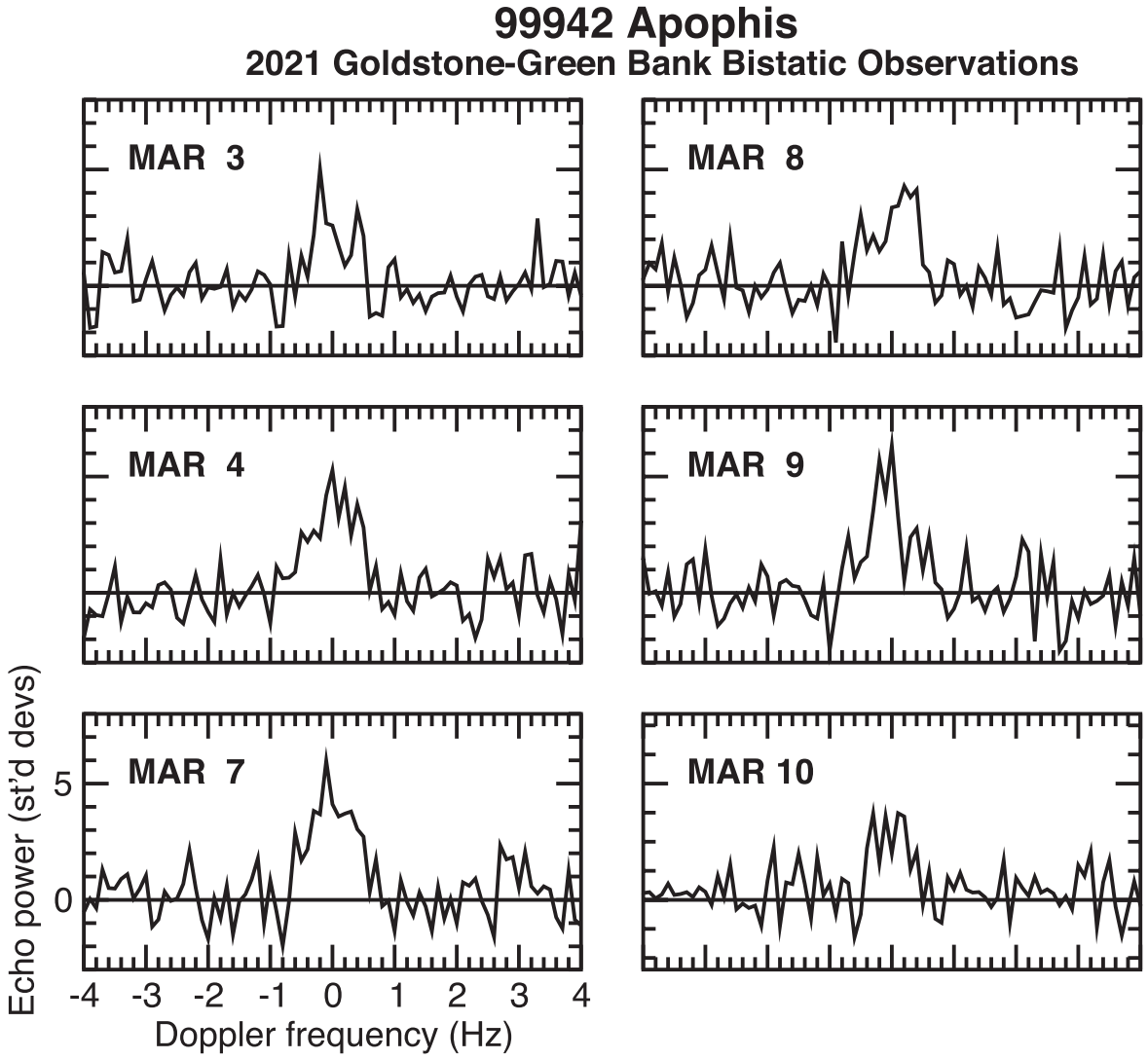

Figure 5. Opposite-circular echo power spectra from Apophis obtained on six days between March 3–10 using Goldstone to transmit and the Green Bank Telescope to receive. In each figure, echo power in standard deviations of the off-echo noise is plotted as a function of Doppler frequency. The resolution is 0.1 Hz, and each figure is shown at the same scale. Dates are indicated in each panel.

data obtained by NASA's NEOWISE spacecraft in December 2020.

The bandwidths evident in the echo power spectra and delay-Doppler images were consistently narrow and changed from ∼1 Hz to ∼1.6 Hz from day to day (Figure 5), implying an object with significant elongation and placing a lower bound on the pole-on dimensions of about 240 m × 460 ± 20% m. A few echoes show a dip in signal strength within the echo (e.g., March 3 and 8 in Figure 5), hinting at the presence of a substantial concavity; these dips are consistent with the appearance of Apophis radar echoes obtained in 2013 (Brozović et al. 2018). However, due to the low S/Ns, these apparent dips are also consistent with variations from receiver noise.

The echoes can constrain the composition of the asteroid through estimates of the radar albedo (the radar cross section normalized by the projected area; Ostro et al. 2002) and, in some instances, the circular polarization ratio (Benner et al. 2008). NEA radar albedos vary between ∼0.05–0.6, where the highest albedos have been measured for metallic objects and the lowest for primitive, optically dark objects (Ostro et al. 2002). Due to issues with data processing, the radar cross sections (and thus the radar albedos) were not estimated until well after the Apophis campaign concluded, but from the weak echo strengths obtained in near real-time, it was clear that the radar albedo was much too low for the asteroid to be metallic and instead favored a rocky surface composition.

The circular polarization ratio is the ratio of echo power in the same sense as the circular polarization that was transmitted relative to echo power in the opposite sense. A reflection from a smooth surface would return most of the echo power in the opposite sense. Among NEOs, measured values for the ratio vary from zero to ∼1.5 with a mean of $0.34 + -0.25$ (Benner et al. 2008). Benner et al. (2008) found that circular polarization ratios >0.6 correlate strongly with the V- and E-taxonomic classes, corresponding to basaltic and enstatite achondrite compositions. For other spectral classes, the ratios are generally <0.5, but otherwise, there are no obvious trends. Inspection of the Apophis echoes indicates a circular polarization ratio of ∼0.2–0.3, significantly less than 0.6, which almost certainly rules out a V- or E-class composition.

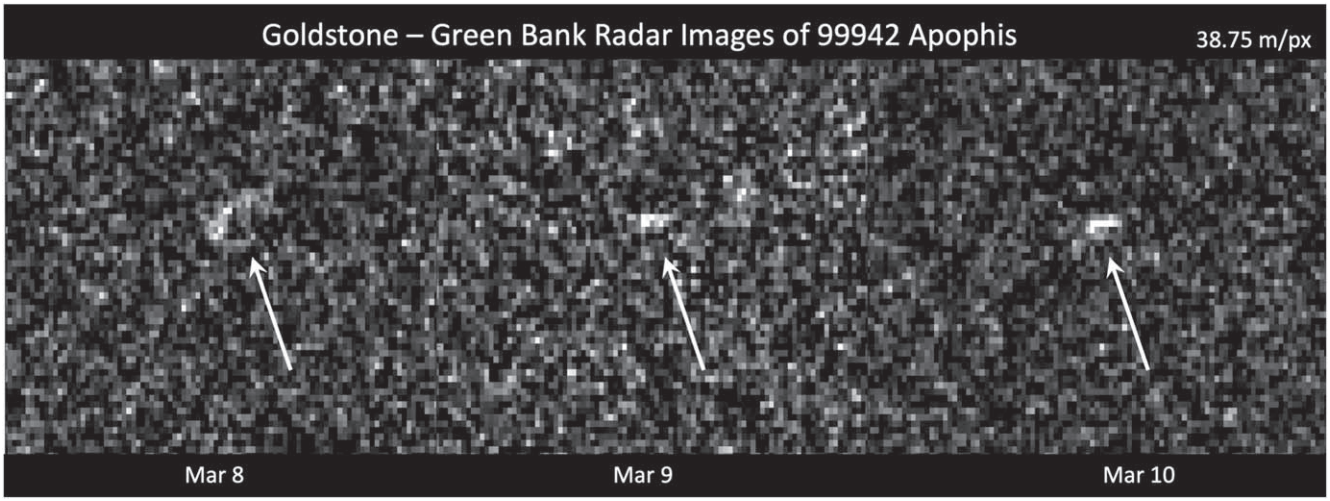

Figure 6. Collage of selected delay-Doppler images obtained on March 8, 9, and 10 using Goldstone to transmit and Green Bank to receive. In each image, time delay (range) increases downward and Doppler frequency increases to the right, so rotation is counterclockwise. Each row corresponds to 37.5 m (0.25 μs). The resolution in Doppler frequency is 0.1 Hz. Each image is an integration spanning about 1 hr and corresponds to about 12 degrees of rotation. The images are shown with the same dimensions in time delay and Doppler frequency.

The S/Ns of the echoes were too weak to obtain detailed delay-Doppler images but were strong enough for coarse-resolution imaging (37.5 m) that revealed the asteroid's orientation, placed constraints on its dimensions, and provided additional information on the shape (Figure 6). The appearance of the images varied slowly during individual observing sessions but differed from day to day. The images show an elongated, asymmetric object that rotates slowly in a manner consistent with the 30.55 hr period estimated from the lightcurves (see Section 5).

The echo extents in time delay (range) allow us to place lower bounds on the pole-on dimensions of roughly 330×220 m. Of course, the asteroid's shape casts a radar shadow, so some of the surface was not illuminated and is thus not visible in the images. In addition, due to the weak S/Ns, echo power from the true trailing edges of the asteroid is down in the noise and not detectable, so the actual dimensions are certainly larger than the lower bounds. These lower bounds are smaller than but consistent with the constraints estimated from bandwidths in the echo power spectra (Figure 5), with the effective diameter of 340 m estimated by Brozović et al. (2018) and with the NEOWISE diameter obtained in this exercise (Section 3.2).

About 15% of NEAs larger than ~200 m in diameter have at least one satellite (Pravec et al. 2006), and for an actual impact, knowing whether the asteroid is a binary or triple could be important. The vast majority of the ~70 known NEA systems with satellites have rapidly rotating primaries with periods of less than 4 hr (Pravec et al. 2006), so based on the slow 30.55 hr period obtained from lightcurves, we did not expect to see evidence for a satellite. The signature of a companion in the echo power spectra would most likely appear as a narrow spike superimposed on a wider echo, a pattern that does not match the Apophis CW data. In delay-Doppler images, a satellite would appear as a separate echo (possibly only one or two pixels in extent) whose position changes with time; no such separate echo is visible in the Apophis images. Thus, the radar observations show no evidence of a satellite.

7. Hypothetical Risk Assessment

Probabilistic methods are a powerful tool for assessing the risk due to asteroid impacts. Mathias et al. (2017); Stokes et al. (2017), and Rumpf et al. (2017) performed a probabilistic risk assessment of the overall risk due to the population of NEAs. A modification of the ensemble risk approach of Mathias et al. (2017) was previously used to assess the hypothetical risk due to a single object as part of the observational campaigns of 2012 TC4 (Reddy et al. 2019) and 1999 KW4 (Reddy et al. 2021). A similar risk assessment was done as part of the Apophis observing campaign.

Four risk assessments were performed to support the Apophis observing campaign. For the purpose of the exercise, no previous knowledge about Apophis was used for the risk assessments. As noted previously, each assessment epoch reflects a significant advancement in the state of knowledge about the impact probability, possible locations of the impacting clone, and the physical properties of Apophis. A summary of the state of knowledge in each epoch is found in Table 4.

The Probabilistic Asteroid Impact Risk (PAIR) model of Mathias et al. (2017) and the affected population metrics defined by Stokes et al. (2017) were used to assess the risk at each epoch. PAIR utilizes a Monte Carlo framework to sample the range of possible impact locations and impactor physical properties. For this exercise, each assessment involved modeling 5000 asteroid property cases striking Earth at each of 5000 hypothetical entry points resulting in 2.5 million simulated impacts at each epoch. Each property case consists of a set of relevant asteroid physical properties that are internally plausible and consistent with the state of knowledge at each epoch. The 5000 asteroid property cases were generated by an inference network that probabilistically samples from distributions of likely asteroid properties based on available measurements, the distribution of the underlying population of NEAs, and likely relationships between the properties. The generation of the hypothetical entry points is described in Section 3. A summary of the state of knowledge in each epoch is found in Tables 4 and 5.

Table 4
Overview of Risk Assessment Epochs

Quantity	Epoch 0	Epoch 1	Epoch 2	Epoch 3
Date of Assessment	23 Dec 2021	23 Dec 2021	22 Jan 2021	19 March 2021
Impact Probability	0.6%	0.6%	6%	100%
H Magnitude	19.3 ± 0.5			
Effective Spherical Diameter		300m ± 75 m	300m ± 75 m	340m ± 50 m
Albedo		0.44 ± 0.19		
Composition			Sq taxonomy; LL chondrite	Sq taxonomy; LL chondrite
Average Affected Population	1.85×10^5	1.2×10^4	1.38×10^5	2.3×10^6
Range of Affected Population	$0–2.6 \times 10^9$	$0–6.1 \times 10^7$	$0–5.4 \times 10^7$	$0–1.96 \times 10^7$

Note. The physical measurements used to define impactor property distributions and the resulting affected population are shown.

Table 5
Timeline of when Different Properties of the Hypothetical Impactor were Determined during the Campaign

Impactor Property	Information Availability Date
"Survey Detection"	04 Dec 2020
"NEOWISE Discovery"	23 Dec 2020
MPC H Mag.	23 Dec 2020
Thermal IR Spherical Diameter	23 Dec 2020
Albedo	23 Dec 2020
Rotation Period	21 Jan 2021
Composition	22 Jan 2021
Radar Diameter	19 Mar 2021

Note. The timeline was constructed after the campaign based on when the information was shared and is the best approximation.

Atmospheric entry and breakup were modeled for each hypothetical case using the Fragment Cloud Model (Wheeler et al. 2017) to calculate the energy deposited in the atmosphere, the effective airburst altitude, any remaining energy striking the ground, and the coordinates of the impact or airburst point along the entry trajectory. The extent of damage resulting from blast waves, thermal radiation, tsunami, and global effects was computed, and the number of people affected was calculated from the local population within the damage regions. For local blast and thermal damage, fractions of the affected population within the exposed regions are evaluated for four damage severity levels: serious (10% population), severe (20% population), critical (60% population), and unsurvivable (100% population). For tsunami, fractions of the population within the inundated region are determined based on flood depth. For global effects, fractions of the total world population are probabilistically sampled from an uncertainty range based on the impactor energy. The total affected population for each case is taken to be the largest population value among all of the hazard sources.

The campaign first discovered Apophis on 2020 December 23 as described in Section 3. In order to provide a baseline, an epoch 0 risk assessment was performed based only on the impact probability, possible hypothetical entry points, and an absolute magnitude provided by the available astrometry measurements. For each of the 5000 property cases, an absolute magnitude was sampled from a Gaussian distribution with a mean of 19.3 and a width of 0.5. All other properties were sampled from the distribution of the overall population of asteroids. An albedo was randomly chosen from the bimodal distribution of albedos of NEAs by Mainzer et al. (2011). The diameter for each case was calculated from the absolute magnitude and albedo using the standard relationship. A likely taxonomy was assigned for each case based on the albedo and a simple application of Bayes theorem $P(T|p_v) \sim P(p_v|T) * P(T)$, where $P(p_v|T)$ is the measured albedo distribution for each taxonomy and $P(T)$ is the distribution of asteroids among the taxonomies. The distributions from DeMeo & Carry (2013) were used for $P(p_v|T)$ and $P(T)$. Each taxonomy was associated with a base density distribution appropriate for the related meteorites. Bulk densities were calculated by modifying the base densities using a broad porosity distribution as presented in Mathias et al. (2017). The aerodynamic strength was distributed uniformly in log space in the range of 0.1–10 MPa. The aerodynamic strength was loosely linked to the porosity by quartiles, with the least porous quartile of cases being associated with the strongest strength quartile. Due to the modest impact probability and wide range of plausible physical properties, the outcome of the risk assessment has a wide range of possible outcomes, ranging from no affected population up to 2.6 billion people. The probability of different ranges of the affected population is shown in Figure 7.

The NEOWISE diameter measurement (300 ± 75 m) and derived albedo (0.44 ± 0.19) were included in the risk assessment for epoch 1. A diameter derived using only the photometry measurements described in Section 5 was consistent with the diameter derived from NEOWISE, but had a larger uncertainty, so the risk assessment used the NEOWISE parameters. To generate 5000 property cases for epoch 1, a large base set of physically plausible property sets were generated as described for epoch 0. From this set of ∼million property cases, a set of 5000 was selected for inclusion in the epoch 1 PAIR risk assessment such that the diameter distribution and albedo distributions matched the NEOWISE measurements of diameter and albedo. The approach of downselecting property cases from the larger set of possibilities generated for the preceding epoch is equivalent to using the state of knowledge from the previous epoch as a statistical prior for the current epoch. Epoch 0 and epoch 1 considered the same impact points and probabilities. The improved state of knowledge of the physical properties resulted in a significant reduction in the uncertainty of the outcomes of the risk assessment. The affected population ranged from 0 to 61 million people with an average of 12,000, which represents an order of magnitude reduction in the average number of affected people.

The epoch 2 risk assessment included two improvements in the state of knowledge based on observations available at that time. The additional astrometry yielded an increased impact probability of 6% and a smaller geographic region of potential

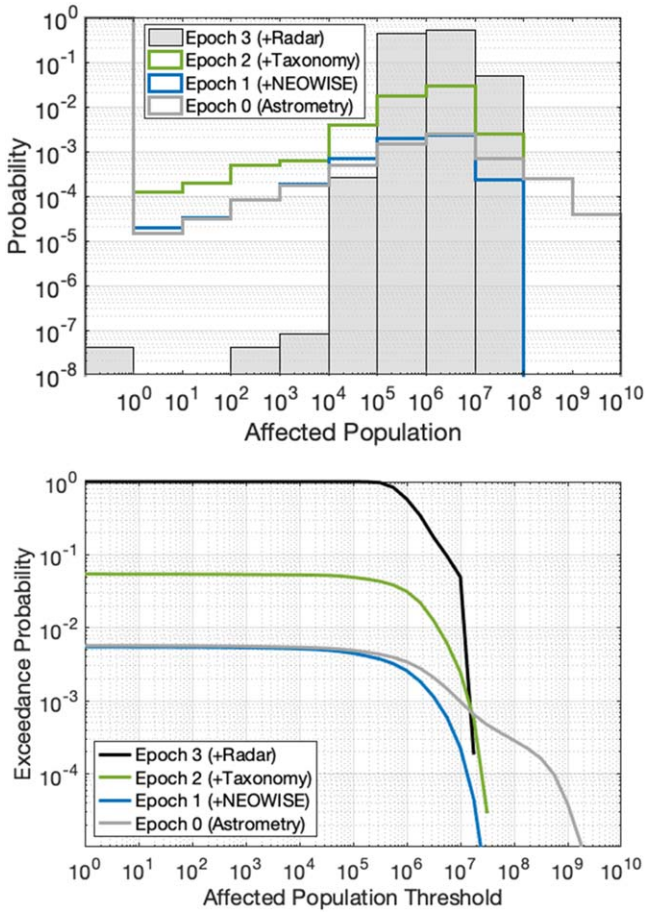

Figure 7. The probability histogram (top) shows how the probability of the impact affecting different orders of magnitude of population evolves over the different epochs. For example, in epoch 3, there is a ~50% chance of affecting between 10^6 and 10^7 people. The complementary cumulative distribution plot (bottom) shows how the probability that a certain population level or more will be affected in each epoch. For example, in epoch 3, there is a 5% chance that 10^7 or more people will be affected.

impacts. The 5000 hypothetical entry points were selected from the revised (smaller) geographic region of potential impacts. In addition, IRTF spectroscopy was used to determine an Sq-type taxonomy with a meteorite LL-chondrite analog. The 5000 property cases were downselected from a larger base set of properties consistent with the epoch 1 state of knowledge. The cases were chosen such that the taxonomy = Sq and the distribution of base densities were consistent with an LL chondrite. In epoch 2, the mean number of the affected population increased to 138,000, largely due to the increase in the impact probability. The full range of affected populations did not change significantly from epoch 1, varying from a minimum of 0 to a maximum of 54 million people.

The epoch 3 risk assessment included improvements in astrometry. At this point, the virtual impactor was assessed to have a 100% impact probability and a much smaller geographic region of possible impacts. In addition, the initial radar results were used to update the estimate of the size. A radar size estimate of $460\,\mathrm{m} \times 240\,\mathrm{m} \pm 20\%$ was provided during the exercise. An effective spherical diameter of $340 \pm 50\,\mathrm{m}$ was derived by allowing the third dimension of the triaxial body to vary between the two provided dimensions, calculating the resulting volume and determining the diameter of a sphere with the same volume. The 5000 property cases were downselected from a larger set, which represented the epoch 2 state of knowledge such that the diameter distribution of the selected cases had the desired distribution of the effective spherical diameter. The average affected population increased to 2,300,000, due both to the 100% impact probability and because the radar size estimate eliminated some smaller objects from the property cases.

The improvements in astrometry described in Section 3 were incorporated into the risk assessment epochs and substantially reduced the uncertainty in possible hypothetical impact locations. Epochs 0 and 1 used the same possible impact locations and impact probability. Epochs 2 and 3 incorporated new astrometry measurements to determine improved estimates of hypothetical impact locations and impact probability. The probability of affecting different population ranges for each epoch due to both improvements in astrometry and knowledge of the hypothetical impactor's properties is shown in Figure 7. The progression of the range of possible hypothetical impact locations is shown in Figure 8.

8. Summary

The Apophis campaign enabled us to learn several key lessons about our preparedness to react to a potential global planetary defense threat. We have summarized these lessons learned by each of the working groups below.

Astrometry (optical, NEOWISE thermal IR, and radar): Within the context of the observation campaign, Apophis was first detected on 2020 December 4, but the pseudo-discovery was announced on 2020 December 23 because of the initially low digest2 score. On the one hand, this delay suggests the need to improve the digest2 score by using a more accurate asteroid population model, a frequently updated census of known asteroids, and accounting for the curvature in the astrometric data. The MPC has already taken steps in this direction (MPEC 2021-G106, https://minorplanetcenter.net/mpec/K21/K21GA6.html). On the other hand, NEOs can often be hard to differentiate from main-belt asteroids at some points in their orbits, and so improvements in linking data in the ITF are certainly warranted. If the Weryk et al. (2018) algorithm had been running more frequently, Apophis would have been identified as early as 2020 December 9. This indicates that a faster version of the Weryk et al. (2018) linking algorithm should be run daily, possibly restricted to tracklets with a moderate digest2 score. To this end, the MPC is working toward implementing HelioLinC (Holman et al. 2018) as part of an automated, daily linking pipeline.

The length of the observed arc is key in reducing orbital uncertainties. For the current campaign, the observing conditions were favorable because Apophis was bright (peak V magnitude 16) and high in the night sky (up to a solar elongation of 156°). As a result, the ongoing surveys provided full astrometric coverage of the flyby while maintaining their operational observation schedule. Under these circumstances, there is more value in the astrometric quality of follow-up observations than in the number of observations, which should generally be limited to no more than four per night per station (Vereš et al. 2017). Timing errors at some sites need to be reduced as they can result in significant systematic errors that bias the trajectory estimate. Calibrating the timing of astrometric images with existing tools (e.g., https://projectpluto.com/gps_expl.htm) is highly recommended. Radar observations proved to be extremely powerful at

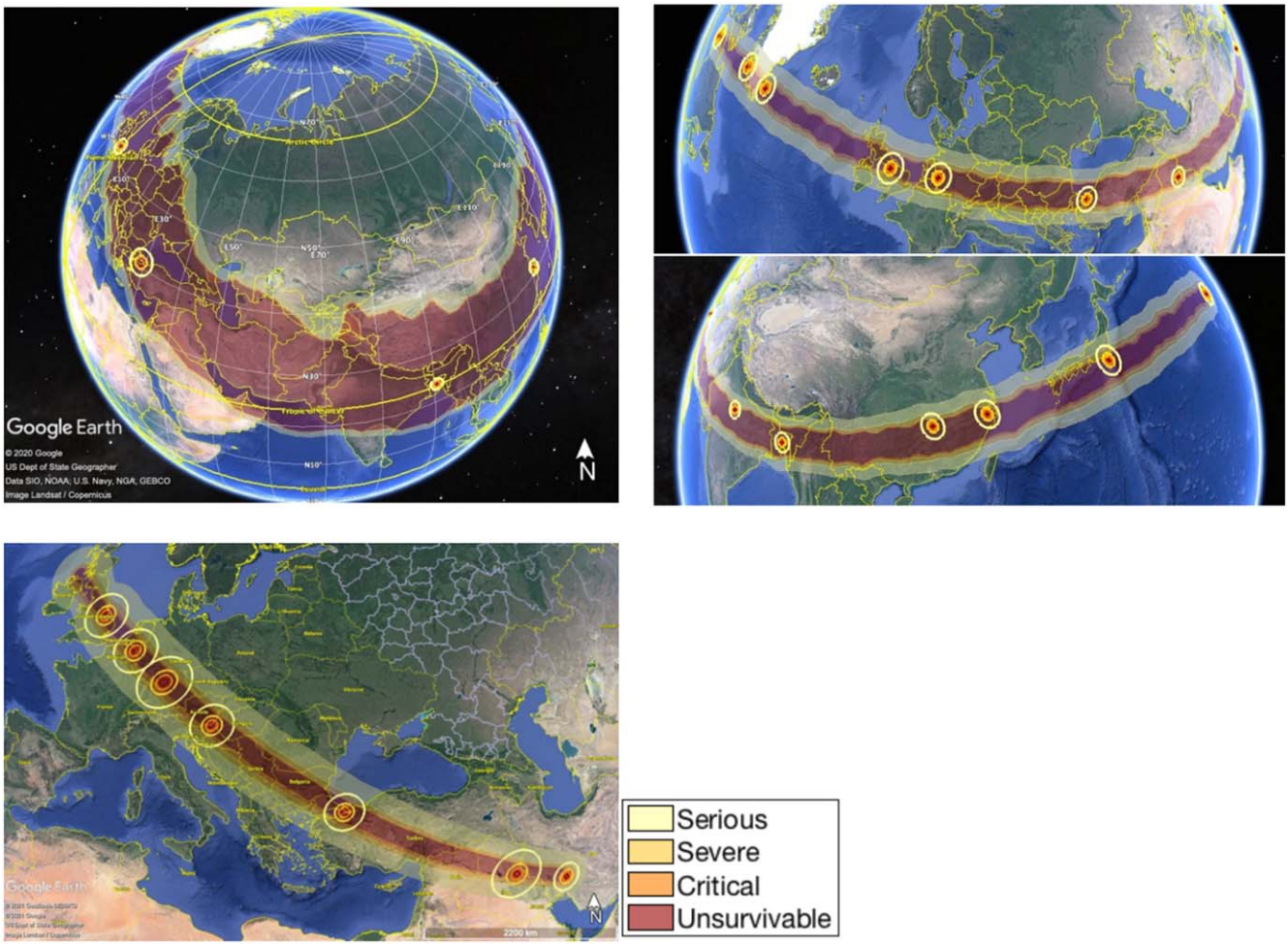

Figure 8. Hypothetical impact swaths for epochs 0/1, 2, and 3. The impact swaths represent all possible considered impact positions and asteroid properties. A hypothetical impact would only occur at one position along the swath, but all possible positions are shown. The rings show the extent of different levels of damage for specific impact locations along the swath.

constraining the orbit due to their high fractional precision and orthogonality to optical measurements.

The pseudo-discovery apparition was unusually favorable because it allowed an observational arc of five months and because Apophis came close enough for radar observations. Moreover, the trajectory of Apophis from 2020 to 2029 has no planetary encounters that could increase prediction uncertainties. Even so, there are limitations on how accurately the impact location can be predicted for a case like this exercise scenario; the impact corridor for the hypothetical impactor still spanned $\pm$1000 km at the end of the campaign. While radar made an important contribution to the astrometry and size estimates, it does require the object to be sufficiently large and make a close approach. If these conditions are not met in a real-world scenario, one is limited to optical astrometric observations for impact prediction.

Rapid characterization of the asteroid's size is an important component in determining its hazard. The different techniques used here present different levels of uncertainty, with >50% for size assumptions based on photometry with spectroscopic taxonomy, ~25% from NEOWISE, and ~20% from radar. Independent from this observation campaign, occultation measurements were obtained for Apophis in 2021 March and April (http://iota.jhuapl.edu/Apophis2021.htm). Occultations can be extremely precise but require an ephemeris with very small uncertainties to succeed and significant deployment efforts. This difficulty has meant that prior to Apophis, the only NEO with an observed stellar occultation was (3200) Phaethon (Dunham et al. 2020). Future planetary defense campaigns should test the feasibility of rapidly assessing occultation opportunities and deploying occultation networks to support additional size and shape characterization of potential impactors.

Photometry: A key lesson learned from the photometry perspective is the impact of human activities on our ability to collect observations. The campaign started on December 24 and coincided with an extensive holiday period for many observers. This is evident in the large gap in photometric follow-up data from the majority of observing sites for the first ~10 days of the campaign. Initially, the only densely sampled photometric data came from the Wise Observatory's 28 inch telescope, with some sparse data coming from the robotic ATLAS observatories. It took about 20 days after the campaign started to derive the principal rotation period (30.55 hr). This was partly because of the initial 10 day "gap" due to the holiday period and also because the lightcurve data that did immediately follow were all from the same location (Wise Observatory; see Table 2). The single location made it difficult to resolve the very slow rotation period and/or rule out ambiguity in the period because the measured period of

30.55 hr is commensurate with the typical diurnal cadence of 24 hr from a single site. Only after data started flowing in from Steward Observatory on Kitt Peak, Arizona, USA (which was at a significantly different longitude relative to the Wise Observatory in Israel) 16 days after the campaign started was the period truly resolved. After this, subsequent data improved the uncertainty in the period and revealed the non-principal-axis rotation state.

Spectroscopy: We investigated the impact of S/N on our ability to accurately classify the Apophis' visible/near-IR spectrum. The near-IR spectrum used for the campaign was noisier (S/N of 40 at ~1 μm, to 20 at ~2.5 μm) compared to reflectance spectra obtained later, when Apophis was brighter ($V_{\rm mag} = 15.5$). This first observation was sufficient to identify Apophis' classification as belonging to the S-complex classification and to provide a rough estimate of its albedo and density from a statistical approach (e.g., Mainzer et al. 2011; Carry 2012). Only by adding the visible range was it possible to further classify Apophis as an Sq type and refute an S- or a Q-type taxonomy. An S/N of at least 30 (at the ~1 μm absorption-band area) is required to distinguish among the S, C, and X complexes (Figure 4(A)), while an S/N of >40 (at ~1 μm) is required to disentangle the subgroups of the S complex: S, Sq, Q types (Figure 4(B)). In addition, the differences in reflectance are larger in the near-IR than in the visible range. This means that any observations taken for the classification of a new asteroid should aim to obtain these levels of S/N using a system capable of measuring near-IR spectroscopy. The IRTF is capable of such a task for an asteroid at a $V_{\rm mag}$ of 18, in a reasonable exposure time of 30–60 minutes.

The visible spectrum that was obtained at GTC on January 26, at $V = 17.3$ mag, provided an S/N of ~120, which is much better than required to identify the taxonomy. This demonstrates the capability of the GTC to provide high-precision spectral measurements of NEAs even at very faint magnitudes. The community of asteroid researchers should secure access to facilities such as the GTC and IRTF and maintain experienced and skilled teams for fast observations, reduction, and analysis.

Hazard modeling: When little is known about a potential impactor, the range of possible outcomes is extremely large, which could complicate mitigation planning and communication. Rapid acquisition and reporting of the physical properties of a potential impactor, such as diameter constraints provided by NEOWISE shortly after discovery, significantly reduced the worst-case outcomes. However, even by the end of the campaign, the impact location uncertainty was still over 1000 km across, showing the limitations when an object is only able to be observed for a few months.

Overall, the campaign successfully demonstrated the capability of the planetary defense community to respond in real time to a potentially impacting object and obtain data sufficient to characterize its orbit, brightness, size, spectrum, rotation period, and hazard to Earth. Timely reporting of astrometry and preliminary physical property analyses, with appropriate error bars, significantly improved our knowledge of the potential impact consequences. Human factors, such as the end-of-year holiday season, had a distinct impact on rapidly constraining the rotation period of Apophis and demonstrate the importance of building a broad coalition for planetary defense spanning continents and cultures. Future planetary defense campaigns should focus on targets with less-favorable apparitions that might better simulate a future discovery of a hazardous object.

Acknowledgments

The Apophis campaign was conducted as part of the International Asteroid Warning Network (IAWN). IAWN is supported by the Planetary Data System (PDS) Small Bodies Node (SBN) at the University of Maryland College Park. The work at the Jet Propulsion Laboratory, California Institute of Technology, was performed under a contract with the National Aeronautics and Space Administration (NASA). This material is based in part on work supported by NASA under the Science Mission Directorate Research and Analysis Programs. This publication makes use of data products from NEOWISE, which is a joint project of the University of Arizona and the Jet Propulsion Laboratory/California Institute of Technology, funded by the Planetary Science Division of NASA. Pan-STARRS is supported by the National Aeronautics and Space Administration under Grant No. 80NSSC18K0971 issued through the SSO Near Earth Object Observations Program. Part of this work was supported by the Russian Ministry of Science and Higher Education via the State Assignment Project FEUZ-2020-0030. Part of the observations performed with the Zeiss-1000 telescope of the Terskol Observatory Shared Research Centre of the Institute of Astronomy of the Russian Academy of Sciences. We are extremely grateful to the IRTF and GTC Observatories' night and day staff for their overwhelming support and assistance that made the observations possible. D.P. & M.M. are thankful to Richard Binzel and Francesca DeMeo for sharing their experience and wisdom while planning and conducting the measurements. D.P. is grateful to the Israeli Space Agency. M.M. was supported by the National Aeronautics and Space Administration under grant No. 80NSSC18K0849 issued through the Planetary Astronomy Program. J.d.L., J.L., and M.P. acknowledge financial support from the NEOROCKS project, which has received funding from the European Union's Horizon 2020 research and innovation program under grant agreement No. 870403. This work was funded by NASA's Planetary Defense Coordination Office. Supercomputing resources supporting this work were provided by the NASA High End Computing (HEC) Program through the NASA Advanced Supercomputing (NAS) Division at Ames Research Center. This work has made use of data from the Asteroid Terrestrial-impact Last Alert System (ATLAS) project. ATLAS is primarily funded to search for NEAs through NASA grants NN12AR55G, 80NSSC18K0284, and 80NSSC18K1575; byproducts of the NEA search include images and catalogs from the survey area. The ATLAS science products have been made possible through the contributions of the University of Hawaii Institute for Astronomy, the Queen's University Belfast, the Space Telescope Science Institute, and the South African Astronomical Observatory. This work is partially supported by the South African National Research Foundation (NRF). Spacewatch is supported by NASA/NEOO grants and the Brinson Foundation of Chicago, IL. We thank TUBITAK National Observatory for partial support in using the T100 telescope with project number 20CT100-1743. This work was supported by the Moscow Center of Fundamental and Applied Mathematics, Agreement with the Ministry of Science and Higher Education of the Russian Federation, No. 075-15-2019-1623. This work made extensive use of Python, specifically the NumPy (Harris et al. 2020), Astropy (Astropy

Collaboration et al. 2013, 2018), Matplotlib (Hunter 2007), and SciPy (Virtanen et al. 2020b) packages.

ORCID iDs

Vishnu Reddy https://orcid.org/0000-0002-7743-3491
Jessie Dotson https://orcid.org/0000-0003-4206-5649
Davide Farnocchia https://orcid.org/0000-0003-0774-884X
Nicolas Erasmus https://orcid.org/0000-0002-9986-3898
Joseph Masiero https://orcid.org/0000-0003-2638-720X
James Bauer https://orcid.org/0000-0001-9542-0953
Miguel R. Alarcon https://orcid.org/0000-0002-8134-2592
Daniel Bamberger https://orcid.org/0000-0002-9138-2942
Larry Denneau https://orcid.org/0000-0002-7034-148X
Aren N. Heinze https://orcid.org/0000-0003-3313-4921
Matthew J. Holman https://orcid.org/0000-0002-1139-4880
Myung-Jin Kim https://orcid.org/0000-0002-4787-6769
Csaba Kiss https://orcid.org/0000-0002-8722-6875
Hee-Jae Lee https://orcid.org/0000-0002-6839-075X
Julia de León https://orcid.org/0000-0002-0696-0411
Javier Licandro https://orcid.org/0000-0002-9214-337X
Michael Marsset https://orcid.org/0000-0001-8617-2425
Marco Micheli https://orcid.org/0000-0001-7895-8209
Shantanu P. Naidu https://orcid.org/0000-0003-4439-7014
András Pál https://orcid.org/0000-0001-5449-2467
Daniel E. Reichart https://orcid.org/0000-0002-5060-3673
Akash Satpathy https://orcid.org/0000-0001-5766-8819
Miquel Serra-Ricart https://orcid.org/0000-0002-2394-0711
Eda Sonbas https://orcid.org/0000-0002-6909-192X
Robert Szakáts https://orcid.org/0000-0002-1698-605X
Patrick A. Taylor https://orcid.org/0000-0002-2493-943X
John L. Tonry https://orcid.org/0000-0003-2858-9657
Richard Wainscoat https://orcid.org/0000-0002-1341-0952
Guy Wells https://orcid.org/0000-0002-6667-6535
Robert Weryk https://orcid.org/0000-0002-0439-9341
Patrick Michel https://orcid.org/0000-0002-0884-1993

References

Astropy Collaboration et al. 2013, A&A, 558, A33
Astropy Collaboration et al. 2018, AJ, 156, 123
Benner, L. A. M., Ostro, S. J., Magri, C., et al. 2008, Icar, 198, 294
Binzel, R. P. 2000, P&SS, 48, 297
Binzel, R. P., DeMeo, F. E., Turtelboom, E. V., et al. 2019, Icar, 324, 41
Binzel, R. P., Rivkin, A. S., Bus, S. J., et al. 2001, M&PS, 36, 1167
Binzel, R. P., Rivkin, A. S., Thomas, C. A., et al. 2009, Icar, 200, 480
Bowell, E., Hapke, B., Domingue, D., et al. 1989, Asteroids II (Tucson, AZ: Univ. Arizona Press), 524
Brozović, M., Benner, L. A. M., McMichael, J. G., et al. 2018, Icar, 300, 115
Carry, B. 2012, P&SS, 73, 98
Chesley, S. R. 2006, in IAU Symp. 229, Asteroids, Comets, Meteors (Cambridge: Cambridge Univ. Press), 215
Chesley, S. R., Chodas, P. W., Milani, A., Valsecchi, G. B., & Yeomans, D. K. 2002, Icar, 159, 423
Christensen, E., Africano, B., Farneth, G., et al. 2018, DPS, 50, 310.10
Dandy, C. L., Fitzsimmons, A., & Collander-Brown, S. J. 2003, Icar, 163, 363
de León, J., Pinilla-Alonso, N., Delbo, M., et al. 2016, Icar, 266, 57
DeMeo, F. E., & Carry, B. 2013, Icar, 226, 723
Dunham, D., Dunham, J., Buie, M., et al. 2020, DPS, 52, 412.01
Dymock, R. 2007, JBAA, 117, 342
Eggl, S., Farnocchia, D., Chamberlin, A. B., et al. 2020, Icar, 339, 113596
Erasmus, N., McNeill, A., Mommert, M., et al. 2018, ApJS, 237, 19
Erasmus, N., Navarro-Meza, S., McNeill, A., et al. 2020, ApJS, 247, 13
Farnocchia, D., Chesley, S. R., Milani, A., et al. 2015, in Asteroids IV, ed. P. Michel et al. (Tucson, AZ: Univ. Arizona Press), 815
Giorgini, J. D., Benner, L. A. M., Ostro, S. J., et al. 2008, Icar, 193, 1
Graham, M. J., Kulkarni, S. R., Bellm, E. C., et al. 2019, PASP, 131, 078001
Harris, A. W. 1998, Icar, 131, 291
Harris, C. R., Millman, K. J., van der Walt, S. J., et al. 2020, Natur, 585, 357
Holman, M. J., Payne, M. J., Blankley, P., et al. 2018, AJ, 156, 135
Hunter, J. D. 2007, CSE, 9, 90
Keys, S., Vereš, P., Payne, M. J., et al. 2019, PASP, 131, 064501
Lomb, N. R. 1976, Ap&SS, 39, 447
Mainzer, A., Bauer, J., Cutri, R. M., et al. 2014, ApJ, 792, 30
Mainzer, A., Grav, T., Bauer, J., et al. 2011, ApJ, 743, 156
Mainzer, A., Grav, T., Masiero, J., et al. 2011, ApJ, 741, 90
Marsden, B. G., & Williams, G. V. 1998, P&SS, 46, 299
Masiero, J. R., Mainzer, A. K., Bauer, J. M., et al. 2020, PSJ, 1, 5
Mathias, D. L., Wheeler, L. F., & Dotson, J. L. 2017, Icar, 289, 106
Milani, A., Chesley, S. R., Sansaturio, M. E., et al. 2005, Icar, 173, 362
Nakamura, T., Noguchi, T., Masahiko, T., et al. 2011, Sci, 333, 1113
Ostro, S. J., Hudson, R. S., Benner, L. A. M., et al. 2002, in Asteroids III, ed. W. F. Bottke, Jr. et al. (Tucson, AZ: Univ. Arizona Press), 151
Polishook, D., Moskovitz, N., DeMeo, F. E., et al. 2014, Icar, 243, 222
Pravec, P., Harris, A. W., Kušnirák, P., et al. 2012, Icar, 221, 365
Pravec, P., Scheirich, P., Ďurech, J., et al. 2014, Icar, 233, 48
Pravec, P., Scheirich, P., Kušnirák, P., et al. 2006, Icar, 181, 63
Reddy, V., Kelley, M. S., Dotson, J., et al. 2022, Icar, 374, 114790
Reddy, V., Kelley, M. S., Farnocchia, D., et al. 2019, Icar, 326, 133
Reddy, V., Sanchez, J. A., Furfaro, R., et al. 2018, ApJ, 155, 140
Rumpf, C. M., Lewis, H. G., & Atkinson, P. M. 2017, GRL, 44, 3433
Scargle, J. D. 1982, ApJ, 263, 835
Seidelmann, P. K. 1977, CeMec, 16, 165
Shevchenko, V. G., & Lupishko, D. F. 1998, SoSyR, 32, 220
Stokes, G., Barbee, B., Bottke, W. F., et al. 2017, Update to Determine the Feasibilityof Enhancing the Search andCharacterization of NEOs, Report of the Near-Earth Object Science Definition Team, NASA, https://cneos.jpl.nasa.gov/doc/2017_neo_sdt_final_e-version.pdf
Tonry, J. L., Denneau, L., Heinze, A. N., et al. 2018, PASP, 130, 064505
Valsecchi, G. B., Milani, A., Gronchi, G. F., et al. 2003, A&A, 408, 1179
Vereš, P., Farnocchia, D., Chesley, S. R., et al. 2017, Icar, 296, 139
Vereš, P., Jedicke, R., Fitzsimmons, A., et al. 2015, Icar, 261, 34
Virtanen, P., Gommers, R., Oliphant, T. E., et al. 2020, Nature Methods, 17, 261
Wainscoat, R., Weryk, R., Ramanjooloo, Y., et al. 2020, DPS, 52, 107.03
Weryk, R., Wainscoat, R. J., Williams, G., et al. 2018, DPS, 50, 304.03
Wheeler, L. F., Register, P. J., & Mathias, D. L. 2017, Icar, 295, 149
Wright, E. L., Eisenhardt, P., Mainzer, A. K., et al. 2010, AJ, 140, 1868